Mechatronics 50 (2018) 134–147

Contents lists available at ScienceDirect

Mechatronics

journal homepage: www.elsevier.com/locate/mechatronics

Integrated observer approach using in-vehicle sensors and GPS for vehicle state estimation☆

Giseo Park[a], Seibum B. Choi[a,*], Dongyoon Hyun[b], Jounghee Lee[b]

[a] Department of mechanical engineering, KAIST, 291 Daehak-ro, Yuseong-gu, Daejeon 34141, Republic of Korea
[b] Hyundai Motor Company, Chassis System Control Development Team, Hyundai-Kia R&D Center, Hwaseong-si, Gyeonggi-do 18280, Republic of Korea

ARTICLE INFO

Keywords:
Vehicle dynamics
State estimation
Extended Kalman filter (EKF)
Sideslip angle
Sensor fusion

ABSTRACT

This paper presents a new method for estimation of vehicle sideslip angle, which is a critical factor in some vehicle chassis control systems. Making use of easily available in-vehicle sensors and a standalone global positioning system (GPS), an integrated observer approach is developed, which includes a sensor offset compensator and two kinds of extended Kalman filters (EKFs) based on a bicycle model and a kinematic model, respectively. To properly combine the outputs of these EKFs, a weighting factor, a function of tire cornering stiffness and tire force, is designed. The observability of each EKF is checked by observability functions of nonlinear systems. As well as the sideslip angle, the longitudinal velocity, heading angle, and tire cornering stiffness are simultaneously estimated by the proposed algorithm. Finally, the performance of the entire system in various driving scenarios is verified using a test vehicle, and the superiority of the integrated observer is confirmed through a comparative study.

1. Introduction

Over the last decades, varieties of mechatronics have been developed by many researchers and industry experts to improve vehicle safety and agility [1]. In particular, the typical mechatronic systems related to both steering maneuver and vehicle lateral motion are electronic stability programs (ESPs) and torque vectoring (TV), which have already been implemented in modern production cars [2]. As well as yaw rate, steering angle, and wheel speed information, vehicle sideslip angle is also necessary for these mechatronic systems to provide both appropriate actuation time and manipulated variables [3]. In fact, since directly measuring the sideslip angle requires very expensive measuring equipment and complex procedures for installation, an estimation algorithm using easily available in-vehicle sensors is desired [4]. Generally, these in-vehicle sensors, such as wheel speed sensors, a gyroscope, an accelerometer, and a steering angle sensor are mounted on production vehicles equipped with ESP [5]. Also, vehicle models categorized as a bicycle model and a kinematic model are utilized for the estimation of sideslip angle. A bicycle model-based estimator is known to produce accurate estimations, but susceptible to vehicle parameter errors [2,6]. Especially, one of main issues of the bicycle model, the estimation of tire cornering stiffness was discussed in some previous works. An adaptive law proposed by Hahn et al. [7] estimated the tire-road friction coefficient (TRFC) as well as the tire cornering stiffness, but it was based on a differential global positioning system (DGPS), too expensive equipment to be commercialized. Hsu et al. [8] developed a novel logic to estimate tire slip angle and friction limit using both steering torque and pneumatic trail model. Nevertheless, the estimation results of tire cornering stiffness were not distinctly represented. A recursive least square (RLS) method to estimate the cornering stiffness was suggested by Nam et al. [9]. However, it was based on the tire force sensor, which is unavailable for conventional vehicles.

In contrast, a kinematic model based-estimator is not affected by the change of vehicle parameters. However, the integration errors due to sensor offset would cause the estimation performance to deteriorate [6]. Using a two-antenna GPS receiver, Ryu and Gerdes [10] proposed kinematic Kalman filters which provide high-update estimates of the vehicle states and the sensor biases, and also compensate for roll effects. However, this two-antenna GPS system requires highly rigorous installation work and additional costs. Also, this high dependence on the GPS may make the estimation accuracy deteriorate under some GPS outage conditions.

Accordingly, in some previous papers, the combination of two estimators was proposed. Cheli et al. [11] implemented a fuzzy-logic procedure to combine them, but there was no solution to the sensor offset problem. The algorithm proposed by Chen and Hsieh [12] had

☆ This paper was recommended for publication by Associate Editor Dr. Amir Khajepour.

* Corresponding author.
E-mail addresses: giseo123@kaist.ac.kr (G. Park), sbchoi@kaist.ac.kr (S.B. Choi), dyhyun@hyundai.com (D. Hyun), jhmail@hyundai.com (J. Lee).

https://doi.org/10.1016/j.mechatronics.2018.02.004
Received 1 September 2017; Received in revised form 30 November 2017; Accepted 4 February 2018
Available online 06 March 2018

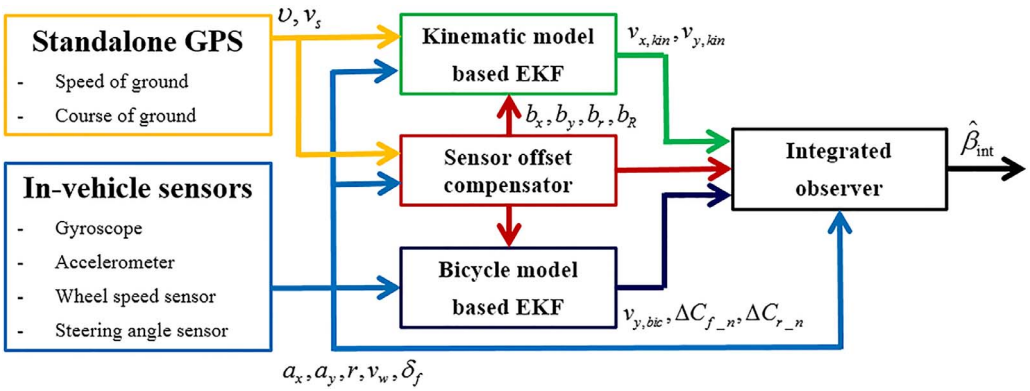

Fig. 1. Flow chart of the integrated observer approach.

the same limitation. Piyabongkarn et al. [13] designed a combination method in which the bicycle model-based estimator was mainly used at low frequencies and the kinematic model-based estimator at high frequencies. However, the estimation performance was limited when large sideslip angles were maintained for a long time period. Oh [2] suggested a multiple-observer approach using a 6-D inertial measurement unit (IMU) and verified its estimation performance, but this approach had the potential to cause excessive computational burden due to its complex structure.

In this paper, a new integrated observer approach for sideslip angle estimation is introduced. In addition to the sideslip angle, other vehicle states such as heading angle, tire cornering stiffness and longitudinal velocity are simultaneously estimated. A flow chart of the integrated observer approach is illustrated in Fig. 1. The combination of the global positioning system (GPS) with data from the in-vehicle sensors is considered [14]. Some researchers stated that this combination was sufficiently accurate and reliable, and had complementary characteristics in terms of accuracy, bandwidth, and noise level [1,6,15–16]. Also, the extended Kalman filter (EKF), an effective method for estimating the states of nonlinear system is utilized for both bicycle model and kinematic model-based estimators.

The main differences distinguishing the proposed algorithm from the previous sideslip angle estimation methods are as follows. First, to prevent the estimation performance from deteriorating, a sensor offset compensator is designed. Due to its simple and intuitive structure, it requires only small computational burden. Second, tire cornering stiffness values in tire nonlinear region are estimated by a bicycle model-based EKF, so that they are usefully utilized to judge and improve the reliability of the bicycle model. Third, in order that an integrated observer combines outputs of two EKFs appropriately, a novel weighting factor is designed, which actively reflects the real-time lateral motion of vehicle. This integrated observer design is applied to multi-model fusion in this paper for the first time. Lastly, because only standalone GPS (in a cost-effective price range) not 6-D IMU is installed additionally, the main advantage of proposed approach is high price competitiveness.

This paper is comprised of six sections. Section 2 describes the used sensors and the algorithm of the sensor offset compensator. Section 3 presents the bicycle model-based EKF with tire cornering stiffness estimation. Then, Section 4 focuses on the kinematic model-based EKF using the combination of GPS and in-vehicle sensors. Section 5 deals with the weighting factor design and the integrated observer. In Section 6, the proposed integrated observer approach is validated experimentally using a test vehicle, and a comparative study is presented. Lastly, conclusions of this study are presented in Section 7.

2. Sensor offset compensator

2.1. Sensors

The speeds of four individual wheel can be obtained from wheel speed sensors. Also, an accelerometer and a gyroscope provide accelerations at the vehicle center of gravity (CG) (i.e. longitudinal a_x and lateral a_y) and yaw rate r, respectively. The data measured from the steering angle sensor can be converted to the front steering wheel angle δ_f with a constant reduction ratio. All data from these in-vehicle sensors are shared by the vehicle controller area network (CAN). In the absence of wheel longitudinal slip, the average of undriven wheel speeds v_w is assumed to be identical to the vehicle longitudinal velocity v_x [2,5–6].

$$v_w = \frac{v_{w,L} + v_{w,R}}{2} \tag{1}$$

The standalone GPS receivers are available in a cost-effective price range [5–6,15,17]. Among the outputs of the GPS, the vehicle speed v_s and course angle ν are used in the proposed algorithm. The principles used in measuring them are the GPS Doppler shifts and the line of sight between vehicle and satellites [14,18]. Here, v_s is the 2-D planar speed, excluding the vertical component (z-axis). Course angle ν represents the direction of the velocity vector in north-east (NE) global coordinates. To express ν in the vehicle body coordinates, a coordinate transformation is performed: the range from 0 to 360° is converted to the range from −270 to 90°.

2.2. Compensation algorithm

There are several reasons for measurement errors in the accelerometer and gyroscope data. Vehicle pitch and roll motions due to severe driving maneuvers or irregular road conditions affect the accuracy of sensors. However, these factors generally result in temporary errors [17,19]. Also, they cannot be measured without additional sensors such as a 6-D IMU. For this reason, they are neglected in this paper. The major cause of the error covered in this paper is a sensor intrinsic offset. This is constantly and consistently included in the sensor output, so that offset compensation is essential to prevent accumulative integration errors. It is assumed that the noise of each sensor is Gaussian white noise.

The offset compensator is designed to be activated only when the vehicle drives straight. The trigger signal with steering commands is simply and intuitively expressed as follows:

$$\varepsilon = \begin{cases} 1 & \text{If } |\delta_f| \le \delta_{f,th} \text{ and } |\dot{\delta}_f| \le \dot{\delta}_{f,th} \\ 0 & \text{otherwise} \end{cases}. \quad (2)$$

The estimated offset of yaw rate, $\hat{b}_r$ is derived as

$$\begin{aligned} r &= r_m + b_r \\ \dot{\hat{b}}_r &= -\varepsilon k_r(\hat{b}_r + r_m). \end{aligned} \quad (3)$$

Here, r_m and k_r are the raw signal and positive tuning gain, respectively. This tuning gain adjusts the convergence speed of offset estimation. In the same manner, the notations mentioned later $a_{x,m}$, $a_{y,m}$ and $v_{w,m}$ are the raw signals, and k_x, k_y and k_w the positive tuning gains. During straight motion ($\varepsilon = 1$), since the reference of the yaw rate is zero, $\hat{b}_r$ converges to a constant value. Otherwise, during the other situation ($\varepsilon = 0$), the estimated value $\hat{b}_r$ is held constant. Similarly, the reference of the lateral acceleration is zero, and the estimated offset of lateral acceleration $\hat{b}_y$ is derived as follows:

$$\begin{aligned} a_y &= a_{y,m} + b_y \\ \dot{\hat{b}}_y &= -\varepsilon k_y(\hat{b}_y + a_{y,m}). \end{aligned} \quad (4)$$

To estimate the offset of longitudinal acceleration $\hat{b}_x$, the vehicle speed measured by the GPS is utilized. During only longitudinal driving, the GPS measurement v_s is almost identical to the vehicle longitudinal velocity v_x regardless of the slip ratio [20]. Therefore, the differential value $\dot{v}_s$, which is processed by a low-pass filter, is considered the reference signal of a_x.

$$\begin{aligned} a_x &= a_{x,m} + b_x \\ \dot{\hat{b}}_x &= -\varepsilon k_x(\hat{b}_x - (\dot{v}_s - a_{x,m})) \end{aligned} \quad (5)$$

As well as the aforementioned sensor offsets, wheel speed errors due to an incorrect value of effective rolling radius R_e (nominal value) have to be compensated. The actual wheel speed v_w can be represented by the measured wheel speed ($v_{w,m} = R_e w_m$) considering the uncertainty of rolling radius b_R:

$$v_w = v_{w,m} + \frac{v_{w,m}}{R_e} b_R. \quad (6)$$

When the vehicle drives straight at constant or slowly varying speed (i.e. $|\dot{v}_s| \le \dot{v}_{s,th}$), the trigger signal ε_w is turned on and the estimated uncertainty of the rolling radius $\hat{b}_R$ converges to a constant value. At this point, the reference of wheel speed is v_s measured by the GPS.

$$\begin{aligned} \frac{v_{w,m}}{R_e}\dot{\hat{b}}_R &= -\varepsilon_w k_w\left(\frac{v_{w,m}}{R_e}\hat{b}_R - (v_s - v_{w,m})\right) \\ \therefore \dot{\hat{b}}_R &= -\varepsilon_w k_w\left(\hat{b}_R - \left(\frac{v_s}{v_{w,m}} - 1\right)R_e\right) \end{aligned} \quad (7)$$

where

$$\varepsilon_w = \begin{cases} 1 & \text{If } |\delta_f| \le \delta_{f,th},\ |\dot{\delta}_f| \le \dot{\delta}_{f,th} \text{ and } |\dot{v}_s| \le \dot{v}_{s,th} \\ 0 & \text{otherwise} \end{cases}.$$

In addition, the outputs of the sensor offset compensator ($\hat{b}_x$, $\hat{b}_y$, $\hat{b}_r$ and $\hat{b}_R$) have to be held constant during the vehicle spin-out condition i.e. $|\cos^{-1}(v_w/v_s)| > \beta_{th}$. They are transmitted to other estimators, and ultimately contribute to improving the accuracy of the sideslip angle estimation.

3. Bicycle model

In the bicycle model, also called the single-track model, it is assumed that the wheels are located at the vehicle center line [21] (see Fig. 2). Therefore, the tire forces of the wheels on both sides are lumped at the center line. The lateral force balance and moment balance equations are formulated in following equations: it is assumed that the longitudinal velocity is constant or changes slowly.

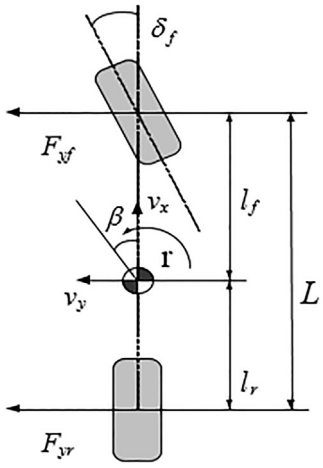

Fig. 2. Diagram of the bicycle model.

$$mv_x(\dot{\beta} + r) = F_{yf} + F_{yr} \quad (8)$$

$$I_z\dot{r} = F_{yf}l_f - F_{yr}l_r \quad (9)$$

where m is the vehicle mass, and I_z the vehicle yaw moment of inertia. Here, l_f and l_r are the CG-front and CG-rear axle distances, and F_{yf} and F_{yr} the lateral tire forces of the front and rear axles, respectively. The wheel slip angles of each axle are expressed as

$$\alpha_f = \beta + \frac{l_f}{v_x}r - \delta_f \quad (10)$$

$$\alpha_r = \beta - \frac{l_r}{v_x}r. \quad (11)$$

The lateral tire force is linearly proportional to the wheel slip angle, and these have opposite signs.

$$F_{yf} = -C_f\alpha_f \quad (12)$$

$$F_{yr} = -C_r\alpha_r \quad (13)$$

where C_f and C_r denote the cornering stiffness of the front and rear axles, respectively. It is assumed that the cornering stiffness is linearly proportional to the tire vertical force, so that C_f and C_r can be normalized by the front and rear vertical forces, respectively [2]. Hence, they are written as the following detailed expressions. At this point, the tire vertical forces can be obtained by the open-loop calculation (if the 6-D IMU is installed additionally, it is possible to consider the roll acceleration effect of the tire vertical force [22]).

$$C_f = (C_{f0,n} + \Delta C_{f,n})F_{zf} \quad (14)$$

$$C_r = (C_{r0,n} + \Delta C_{r,n})F_{zr} \quad (15)$$

where

$$F_{zf} = \frac{mgl_r - mha_x}{l_f + l_r},\ F_{zr} = \frac{mgl_f + mha_x}{l_f + l_r}.$$

Here, h is the height of CG, and the normalized cornering stiffness (C/F_z) is divided into the nominal parameter $C_{0,n}$ and unknown variable

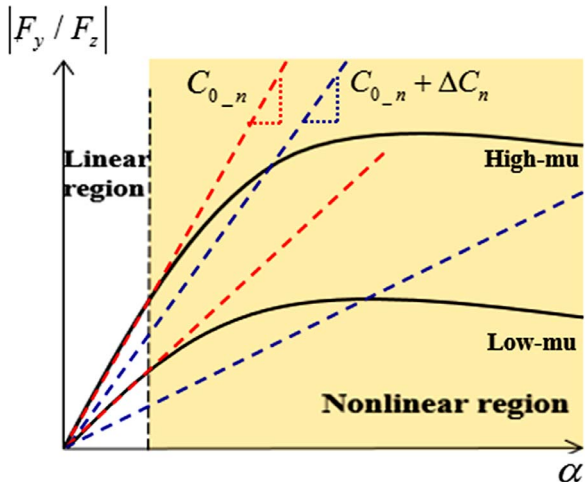

Fig. 3. Normalized lateral tire force versus wheel slip angle.

ΔC_n. The nominal parameter is the slope in the linear region of the normalized lateral tire force, as shown in Fig. 3. But, it cannot be denied that fixed C_{0n} without any adaptation in the nonlinear region reduces the accuracy of lateral tire forces in Eqs. (12) and (13) [2]. When the nonlinear region is reached, the slope decreases. The unknown variable ΔC_n can be expressed as the change of slope. The nominal parameter C_{0n} also varies with the types of road surface. Thus, the lower the TRFC μ is, the smaller C_{0n} is [23]. To be robust to this road uncertainty, the unknown variables $\Delta C_{f.n}$ and $\Delta C_{r.n}$, i.e. the changes of the cornering stiffness are estimated by the bicycle model-based EKF. Also, it is assumed that an adaptive law proposed by Han et al. [24] using only wheel speed signals estimates the real-time μ in advance. Consequently, the nominal parameters matched with the corresponding μ can be predetermined as $C_{f0.n}$ and $C_{r0.n}$.

3.1. Bicycle model-based EKF

The bicycle model-based EKF taking into account the cornering stiffness variation was designed earlier [23]. However, a modified EKF is proposed in this paper, and the features that distinguish it from the previous method are as follows. 1) Because the cornering stiffness is normalized by the tire vertical force in advance, the unknown variable ΔC_n estimated by the EKF can be used to detect the tire nonlinear region in Fig. 3. 2) The yaw rate is added to the state vector of the EKF. Therefore, this addition contributes to improving the estimation performance of EKF. 3) The lateral tire forces F_{yf} and F_{yr} in the measurement vector are easily obtained from simple calculations.

The basic idea of the EKF is a recursive linearization of the system equation around the estimated state. The EKF provides an optimal state estimation in nonlinear systems [25]. Consider the following discrete system model (using a first-order Euler approximation, a differential equation is discretized).

$$x_k = f(x_{k-1}, u_k) + w_k,\ z_k = h(x_k, u_k) + v_k \tag{16}$$

Here, x is the state vector, u the input vector and z the measurement vector; w and v are the process and measurement noises, respectively (assumed to be Gaussian white noise). Detailed procedures of the EKF are described in [26].

By augmenting Eqs. (8)-(15), the state vector and model equation of the bicycle model-based EKF are derived as follows:

$$x_k = [\beta_k \quad r_k \quad \Delta C_{f.n,k} \quad \Delta C_{r.n,k}]^T \tag{17}$$

$$f(x_{k-1}, u_k) = \begin{bmatrix} \beta_{k-1} \\ r_{k-1} \\ \Delta C_{f.n,k-1} \\ \Delta C_{r.n,k-1} \end{bmatrix} + T_s \begin{bmatrix} -\frac{\left(C_{f0.n}+\Delta C_{f.n,k-1}\right)F_{zf}+(C_{r0.n}+\Delta C_{r.n,k-1})F_{zr}}{mv_x}\beta_{k-1} \\ +\left(\frac{(C_{r0.n}+\Delta C_{r.n,k-1})F_{zr}l_r-\left(C_{f0.n}+\Delta C_{f.n,k-1}\right)F_{zf}l_f}{mv_x^2}-1\right)r_{k-1} \\ +\frac{\left(C_{f0.n}+\Delta C_{f.n,k-1}\right)F_{zf}}{mv_x}\delta_f \\ \frac{(C_{r0.n}+\Delta C_{r.n,k-1})F_{zr}l_r-\left(C_{f0.n}+\Delta C_{f.n,k-1}\right)F_{zf}l_f}{I_z}\beta_{k-1} \\ -\frac{\left(C_{f0.n}+\Delta C_{f.n,k-1}\right)F_{zf}l_f^2+(C_{r0.n}+\Delta C_{r.n,k-1})F_{zr}l_r^2}{I_zv_x}r_{k-1} \\ +\frac{\left(C_{f0.n}+\Delta C_{f.n,k-1}\right)F_{zf}l_f}{I_z}\delta_f \\ 0 \\ 0 \end{bmatrix} \tag{18}$$

where

$$u_k = [F_{zf} \quad F_{zr} \quad \delta_f]^T.$$

Here, T_s represents the sampling period. The covariance matrix of process noise is obtained as $Q_{bic} = diag(3.5 \times 10^{-6}, 8 \times 10^{-5}, 3, 3)$, based on the bicycle model characteristics. To increase the sensitivity of cornering stiffness estimation, it can be increased up to $diag(3.5 \times 10^{-6}, 8 \times 10^{-5}, 9, 9)$. Accordingly, the slop of graph in Fig. 3 can be changed more sensitively. The measurement vector and output equation are expressed as

$$z_k = [F_{yf} \quad F_{yr} \quad r]^T$$

$$h(x_k, u_k) = \begin{bmatrix} -(C_{f0.n} + \Delta C_{f.n,k})F_{zf}\left(\beta_k + \frac{l_f r_k}{v_x} - \delta_f\right) \\ -(C_{r0.n} + \Delta C_{r.n,k})F_{zr}\left(\beta_k - \frac{l_r r_k}{v_x}\right) \\ r_k \end{bmatrix} \tag{19}$$

where

$$F_{yf} = \frac{ml_r a_y + I_z\dot{r}}{l_f + l_r},\ F_{yr} = \frac{ml_f a_y - I_z\dot{r}}{l_f + l_r}.$$

Here, the derivatives of the yaw rate in F_{yf} and F_{yr} are processed by the low pass filter. To minimize the effect of noise statistically, the covariance matrix of measurement noise is obtained as

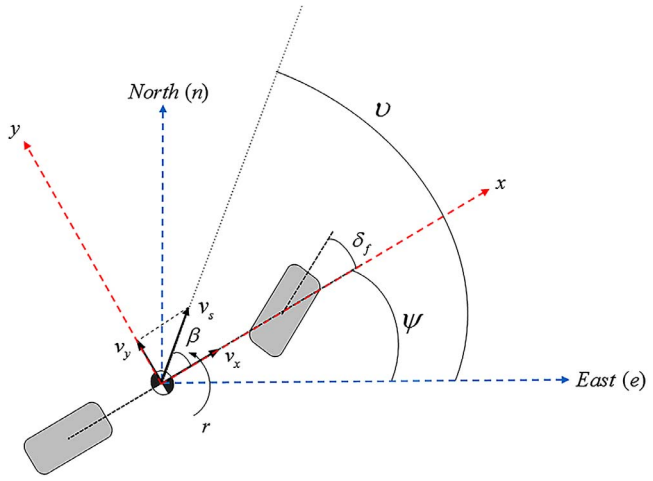

Fig. 4. Diagram of the vehicle kinematic model.

$R_{bic} = diag(3.2 \times 10^4, 6.94 \times 10^4, 5.8 \times 10^{-6})$, based on the sensor noise characteristics. Lastly, the Jacobian matrices F and H of the bicycle model-based EKF are

$$F_k = \left.\frac{\partial f}{\partial x}\right|_{\hat{x}_{k-1},u_k} = I_{4\times4} + T_s \left[\begin{array}{cccc} \frac{\left(C_{f0n}+x_3\right)F_{zf}+(C_{r0n}+x_4)F_{zr}}{mv_x} & \left(\frac{(C_{r0n}+x_4)F_{zr}l_r-\left(C_{f0n}+x_3\right)F_{zf}l_f}{mv_x^2}-1\right) & -\frac{F_{zf}}{mv_x}\left(x_1+\frac{l_f x_2}{v_x}-\delta_f\right) & -\frac{F_{zr}}{mv_x}\left(x_1-\frac{l_r x_2}{v_x}\right) \\ \frac{(C_{r0n}+x_4)F_{zr}l_r-\left(C_{f0n}+x_3\right)F_{zf}l_f}{I_z} & \frac{\left(C_{f0n}+x_3\right)F_{zf}l_f^2+(C_{r0n}+x_4)F_{zr}l_r^2}{I_z v_x} & -\frac{F_{zf}l_f}{I_z}\left(x_1+\frac{l_f x_2}{v_x}-\delta_f\right) & \frac{F_{zr}l_r}{I_z}\left(x_1-\frac{l_r x_2}{v_x}\right) \\ 0 & 0 & 0 & 0 \\ 0 & 0 & 0 & 0 \end{array}\right]\Bigg|_{x=\hat{x}_{k-1}} \tag{20}$$

$$H_k = \left.\frac{\partial h}{\partial x}\right|_{\hat{x}_k,u_k} = \left[\begin{array}{cccc} -(C_{f0n}+x_3)F_{zf} & -(C_{f0n}+x_3)F_{zf}\frac{l_f}{v_x} & -F_{zf}\left(x_1+\frac{l_f x_2}{v_x}-\delta_f\right) & 0 \\ -(C_{r0n}+x_4)F_{zr} & (C_{r0n}+x_4)F_{zr}\frac{l_r}{v_x} & 0 & -F_{zr}\left(x_1-\frac{l_r x_2}{v_x}\right) \\ 0 & 1 & 0 & 0 \end{array}\right]\Bigg|_{x=\hat{x}_k}. \tag{21}$$

Consider the Lie derivative functions L_f and observability function O_{bic} in terms of Eqs. (18) and (19) as below [27].

$$\begin{aligned} L_f^{(0)} &= h \\ L_f^{(i)} &= \frac{\partial L_f^{(i-1)}}{\partial x} \cdot fi = 1, 2, 3 \\ O_{bic} &= \left[\frac{\partial L_f^{(0)}}{\partial x} \;\; \frac{\partial L_f^{(1)}}{\partial x} \;\; \frac{\partial L_f^{(2)}}{\partial x} \;\; \frac{\partial L_f^{(3)}}{\partial x}\right]^T \end{aligned} \tag{22}$$

Because the observability function has a full rank of 4, this nonlinear system of the bicycle model is locally observable. From the wheel speed and estimated sideslip angle, the estimated lateral velocity of the bicycle model-based EKF can be obtained: $\hat{v}_{y,bic} = v_w tan(\hat{\beta}_{bic})$. The outputs of the bicycle model-based EKF play important roles. As shown in Fig. 3, large $\Delta\hat{C}_{f,n}$ and $\Delta\hat{C}_{r,n}$ correspond to the nonlinear region where the reliability of the bicycle model decreases more than that of the kinematic model. In contrary, $\Delta\hat{C}_{f,n}$ and $\Delta\hat{C}_{r,n}$ are generally small in the linear region of lateral tire force. In this case, the bicycle model is known to be highly accurate, and it is wise to utilize $\hat{v}_{y,bic}$ from the bicycle model-based EKF as much as possible. In conclusion, the integrated observer can determine how much to utilize $\hat{v}_{y,bic}$ through $\Delta\hat{C}_{f,n}$ and $\Delta\hat{C}_{r,n}$.

4. Kinematic model

As mentioned above, the kinematic model is robust against changes in the vehicle parameters (mass, yaw moment of inertia, tire cornering stiffness, etc.), type of road surface, and driving operations [13]. Fig. 4 shows the vehicle kinematic model with both vehicle body coordinates for the in-vehicle sensors and NE global coordinates for the GPS. Note that the subscripts denote their corresponding coordinates: (x, y) vehicle body coordinates and (e, n) global coordinates. Here, v_y is the vehicle lateral velocity, and ψ the vehicle yaw angle (also called the heading angle). Both the vehicle speed and the course angle measured by the GPS can be expressed with respect to the vehicle body coordinates.

$$v_s = \sqrt{v_x^2 + v_y^2} \tag{23}$$

$$\upsilon = \psi + \beta = \psi + tan^{-1}\left(\frac{v_y}{v_x}\right) \tag{24}$$

Although the offsets of in-vehicle sensors are estimated and eliminated by the compensation algorithm in Section 2, some factors leading to the integral drift phenomenon still exist, such as an approximation error due to signal discretization, incorrect integral initial value, and unexpected disturbance. To overcome these problems, the use of the GPS measurements, which are free from sensor offset issues, can be a sufficiently effective solution.

4.1. Kinematic model-based EKF

Similar to the Section 3.1, the state vector and model equation of the kinematic model-based EKF are given as follows:

$$x_k = [v_{x,k} \;\; v_{y,k} \;\; \psi_k]^T \tag{25}$$

$$f(x_{k-1}, u_k) = \begin{bmatrix} v_{x,k-1} \\ v_{y,k-1} \\ \psi_{k-1} \end{bmatrix} + T_s \begin{bmatrix} r v_{y,k-1} + a_x \\ -r v_{x,k-1} + a_y \\ r \end{bmatrix} \tag{26}$$

where

$u_k = [a_x \;\; a_y \;\; r]^T$.

Then, the measurement vector and output equation are written as follows:

$$\begin{aligned} z_k &= [v_w \;\; v_{e,GPS} \;\; v_{n,GPS}]^T \\ h(x_k) &= \begin{bmatrix} v_{x,k} \\ v_{x,k}\cos(\psi_k) - v_{y,k}\sin(\psi_k) \\ v_{x,k}\sin(\psi_k) + v_{y,k}\cos(\psi_k) \end{bmatrix} \end{aligned} \tag{27}$$

where the velocity components in the NE global coordinates $v_{e,\ GPS}$ and $v_{n,\ GPS}$ are

$v_{e,GPS} = v_s\cos(\upsilon)$, $v_{n,GPS} = v_s\sin(\upsilon)$.

The Jacobian matrices of the kinematic model-based EKF are derived as below.

$$F_k = \left.\frac{\partial f}{\partial x}\right|_{\hat{x}_{k-1},u_k} = I_{3\times3} + T_s \begin{bmatrix} 0 & r & 0 \\ -r & 0 & 0 \\ 0 & 0 & 0 \end{bmatrix} \tag{28}$$

$$H_k = \left.\frac{\partial h}{\partial x}\right|_{\hat{x}_k} = \begin{bmatrix} 1 & 0 & 0 \\ \cos(x_3) & -\sin(x_3) & -x_1\sin(x_3) - x_2\cos(x_3) \\ \sin(x_3) & \cos(x_3) & x_1\cos(x_3) - x_2\sin(x_3) \end{bmatrix}\Bigg|_{x=\hat{x}_k} \tag{29}$$

The observability function O_{kin} in terms of the Eqs. (26) and (27) has a full rank of 3, so that this system is locally observable [28]. As mentioned above, it is certainly wise to utilize the kinematic model in the nonlinear region of the lateral tire force [2].

As well as the estimated lateral velocity $\hat{v}_{y,kin}$, the estimated heading

angle $\hat{\psi}$ is a noticeable output of the kinematic model-based EKF. Since the heading angle is important information for predicting the next traveling direction of the vehicle, it can be used for various applications from safety control systems (e.g. intelligent airbag systems to minimize collision damage and collision avoidance systems) to autonomous driving systems.

Actually, the accuracy of standard GPS significantly deteriorates under some GPS outage conditions, such as use in tunnels or urban areas with many tall buildings [5]. In this case, it is desirable to replace the kinematic model-based EKF with an open-loop estimator that does not use any GPS measurements. From the number of satellites associated with the accuracy of the GPS measurements, the use of the open-loop estimator can be determined [5].

5. Integrated observer

5.1. Weighting factor design

The integrated observer located at the end of the overall algorithm synthesizes the EKFs in Sections 3.1 and 4.1. Finding the appropriate weighting factor in real time is an important task in determining the performance of the integrated observer approach. Firstly, the sub-weighting factors of front and rear axles are defined as follows.

$$\begin{aligned} K_f &= sat\left[\frac{1}{2\varepsilon_f}(|\Delta C_{f,n}| - \tau_f + \varepsilon_f)\right] \\ K_r &= sat\left[\frac{1}{2\varepsilon_r}(|\Delta C_{r,n}| - \tau_r + \varepsilon_r)\right] \end{aligned} \tag{30}$$

Here, τ and ε are the positive tuning constants that make up the saturation functions. Fig. 5 shows how these sub-weighting factors are formulated as a function of the unknown variable ΔC_n (i.e. change of normalized cornering stiffness). A large ΔC_n results in a high sub-weighting factor; this implies that the reliability of $v_{y,\ bic}$ from the bicycle model-based EKF decreases. In this case, the portion of $v_{y,\ kin}$ has to be raised. On the other hand, a small ΔC_n signifies that the bicycle model is highly accurate and the kinematic model-based EKF is no longer necessary.

Use of the kinematic model-based EKF corresponds with high lateral acceleration (i.e. high normalized lateral force F_y/F_z). Therefore, the final weighting factor $K \in \{K | 0 \le K \le 1\}$ reflecting this tendency is designed as follows:

$$K = \frac{1}{\mu}\max\left(\frac{F_{yf}}{F_{zf}}K_f, \frac{F_{yr}}{F_{zr}}K_r\right). \tag{31}$$

Here, the normalized lateral forces of front and rear axles F_{yf}/F_{zf} and F_{yr}/F_{zr} are obtained from the simple calculation:

$$\frac{F_{yf}}{F_{zf}} = \frac{ml_r a_y + I_z\dot{r}}{mgl_r - mha_x}, \frac{F_{yr}}{F_{zr}} = \frac{ml_f a_y - I_z\dot{r}}{mgl_f + mha_x}. \tag{32}$$

Since the weighting factor K is based on the maximum function ($\max(\bullet, \bullet)$), it can be quickly increased whenever $v_{y,\ kin}$ from the kinematic model-based EKF is highly required. An unnecessary increase of K at low lateral acceleration can be naturally inhibited. Also, by dividing by μ(from the estimation algorithm), the sensitivity of the weighting factor can be maintained even on the low-μ surface. It implies that $v_{y,\ kin}$ gets more weight on the slippery road [29]. Compared with the previous weighting methods [2,13,30], this newly designed weighing factor more actively reflects the real-time lateral dynamics of a vehicle, such as normalized lateral tire force and cornering stiffness. In the next Section 5.2, the weighting factor is used to develop the integrated observer.

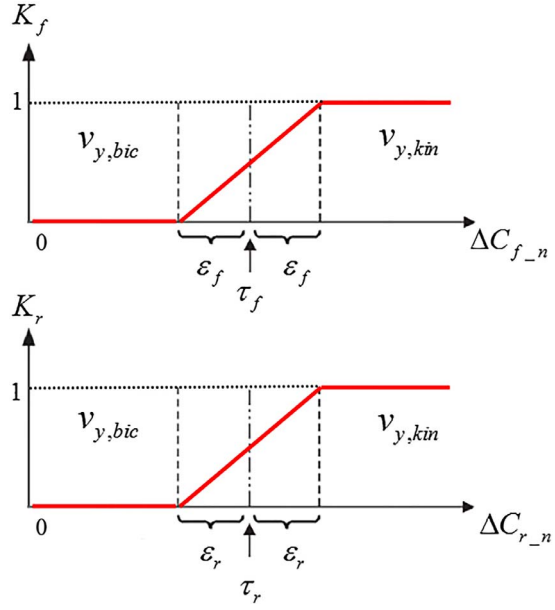

Fig. 5. Weighting factor design.

5.2. Observer design

To incorporate two EKFs based on the bicycle and kinematic models, the integrated observer is proposed in this section. It is identical to the EKF algorithm, so that the above-mentioned EKF process is repeated again. The model equation in terms of $x_k = [v_{x,k} \quad v_{y,k} \quad r_k]^T$ and $u_k = [a_x \quad a_y \quad \delta_f]^T$ is derived as follows:

$$\begin{aligned} f(x_{k-1}, u_k) = &\begin{bmatrix} v_{x,k-1} \\ v_{y,k-1} \\ r_{k-1} \end{bmatrix} + (1-K)T_s \begin{bmatrix} 0 \\ -\frac{C_f + C_r}{mv_{x,k-1}}v_{y,k-1} + \left(\frac{C_r l_r - C_f l_f}{mv_{x,k-1}} - v_x\right)r_{k-1} + \frac{C_f}{m}\delta_f \\ \frac{C_r l_r - C_f l_f}{I_z v_{x,k-1}}v_{y,k-1} - \frac{C_f l_f{}^2 + C_r l_r{}^2}{I_z v_{x,k-1}}r_{k-1} + \frac{C_f l_f}{I_z}\delta_f \end{bmatrix} \\ &+ KT_s \begin{bmatrix} r_{k-1}v_{y,k-1} + a_x \\ -r_{k-1}v_{x,k-1} + a_y \\ 0 \end{bmatrix} \end{aligned} \tag{33}$$

where the tire cornering stiffness $C_{\bullet}$ is equal to $(C_{\bullet,0n} + \Delta C_{\bullet,n})F_{z\bullet}$. On the right-side of Eq. (33), the first and second terms correspond to the bicycle model and kinematic model, respectively. Then, the measurement vector and output equation of the integrated observer are given as follows.

$$\begin{aligned} z_k &= [(1-K)v_w + Kv_{x,kin} \quad (1-K)v_{y,bic} + Kv_{y,kin} \quad r]^T \\ h(x_k) &= [v_x \quad v_y \quad r]^T \end{aligned} \tag{34}$$

These measurements are the weighted sum of the estimated results from two EKFs, not conventional forms of measurement. The Jacobian matrices of the integrated observer are obtained as follows:

$$\begin{aligned} F_k &= \left.\frac{\partial f}{\partial x}\right|_{\hat{x}_{k-1}, u_k} \\ &= \begin{bmatrix} 0 & Kx_3 & Kx_2 \\ -\frac{(1-K)(C_r l_r - C_f l_f)x_3}{mx_1^2} & -\frac{(1-K)(C_f + C_r)}{m} & \frac{(1-K)(C_r l_r - C_f l_f)}{mx_1} - x_1 \\ -\frac{(1-K)(C_r l_r - C_f l_f)x_2}{I_z x_1^2} + \frac{(1-K)(C_f l_f{}^2 + C_r l_r{}^2)x_3}{I_z x_1^2} & \frac{(1-K)(C_r l_r - C_f l_f)}{I_z x_1} & -\frac{(1-K)(C_f l_f{}^2 + C_r l_r{}^2)}{I_z x_1} \end{bmatrix}\Bigg|_{x=\hat{x}_{k-1}} \end{aligned} \tag{35}$$

$$H_k = \left.\frac{\partial h}{\partial x}\right|_{\hat{x}_k} = I_{3\times 3}. \tag{36}$$

The observability function O_{int} in terms of the Eqs. (33) and (34) has a full rank of 3, so that this system is locally observable. Through the stability analysis of the general EKF demonstrated by Reif et al. [31], the exponential stability of the EKF with several assumptions was proven. Lastly, the integrated observer results in the estimated velocities $\hat{v}_{x,\text{int}}$ and $\hat{v}_{y,\text{int}}$, and in doing so, the estimated sideslip angle $\hat{\beta}_{\text{int}}$ $(= \tan^{-1}(\hat{v}_{y,\text{int}}/\hat{v}_{x,\text{int}}))$, the primary outcome of this research is generated. Compared with the simple weighting sum $(\hat{\beta} = (1-K)\hat{\beta}_{bic} + K\hat{\beta}_{kin})$, some advantages of the integrated observer are as follows. 1) The predicted state vector $\hat{x}^-$ of the EKF contributes to higher accuracy. 2) The simple weighting sum may include high frequency noises, whereas the integrated observer eliminates them without any phase lag issues.

Showing the flow chart in Fig. 1, the proposed approach proceeds only in the forward direction, Therefore, both bicycle model and kinematic model-based EKFs do not use the outputs of the integrated observer. Accordingly, although $\hat{\beta}_{\text{int}}$ is inaccurately estimated, the model-based EKFs are not affected by this incorrect $\hat{\beta}_{\text{int}}$ and are able to generate their outputs $\hat{v}_{y,bic}$ and $\hat{v}_{y,kin}$ to recovery this inaccuracy.

6. Experiments

6.1. Experimental set-up

A real production vehicle, Hyundai LF Sonata (midsize vehicle) is utilized for verification of the proposed algorithm. The vehicle specifications are detailed in Table 1. As mentioned above, both TRFC and initial cornering stiffness are predetermined by the TRFC estimation algorithm [24,32]. Fig. 6 shows photographs of the test vehicle and of the RT3002. The RT3002 (from Oxford Technical Solutions, Ltd.) is based on a highly efficient differential GPS (DGPS) system, so that it is accurate enough to measure the actual vehicle states such as vehicle velocities and heading angles. It is assumed that the RT3002 is located at CG of the vehicle. A standalone GPS receiver (for estimation purposes) and DGPS antenna of the RT3002 (for verification purposes) are mounted on the roof of the vehicle. The distance between the roof and the RT3002 is approximately 600 mm.

Using a Micro-Autobox, all of the data from GPS receiver, in-vehicle sensors, and RT3002 are monitored in real time [33,34]. The integrated observer approach is built into the Micro-Autobox. The sampling periods of each sensor are as follows: 1 ms for RT3002, 10 ms for in-vehicle sensors, and 50 ms for standalone GPS. Then, the sampling period of the sideslip angle estimation algorithm, T_s is identical to that of the in-vehicle sensors. Experiments are conducted at the test-drive course of Hyundai-Kia R&D center [35,36], where the accuracy of the GPS is reliable due to the open-sky environment. The test driving scenarios are listed in Table 2. From a variety of driving maneuvers, the effectiveness of the integrated observer approach proposed in this paper can be verified. Especially, the robustness of the algorithm on the slippery surface is evaluated in the experimental case 5.

Table 1
The specifications of test vehicle.

Parameter	Quantity	Value
m	Vehicle mass + people	1819 kg
l_f	CG-front axle distance	1.265 m
l_r	CG-rear axle distance	1.54 m
I_z	Yaw moment of inertia	3566 kg m^2
R_e	Effective rolling radius of tire	330 mm
h	Height of CG	542 mm
C_{f0}	Initial tire cornering stiffness of front axle	191000 N/rad ($\mu \approx 1$) 23500 N/rad ($\mu \approx 0.3$)
C_{r0}	Initial tire cornering stiffness of rear axle	161000 N/rad ($\mu \approx 1$) 18000 N/rad ($\mu \approx 0.3$)

6.2. Experimental results

6.2.1. Experimental case 1

In this test, severe sine steering with a frequency of 3 Hz and maximum amplitude of 50° is conducted. Firstly, the estimation results of the sensor offsets are all shown together in Fig. 7. During the first 3 seconds, the trigger signal for offset estimation in Eq. (2) is turned on, and the estimated offsets converge to constant values. After the vehicle engages in the sine steering maneuver, the trigger signal is turned off, and the estimated offset values are exploited to compensate for the offset errors. As shown in Figs. 7(e), (f), and (i), there are two kinds of absolute errors made by the raw and compensated measurements. Also, the absolute differences between actual v_x and v_w are shown in Fig. 7(j). Although the irregular noise components still exist, it is confirmed that the absolute errors of the compensated measurements are closer to zero. Although this offset compensation is impossible to make the measurement errors zero, it can contribute to improving the accuracy of the sideslip angle estimation.

Fig. 8 shows other results, such as the estimated cornering stiffness values and weighting factor. Since the tire slip angle of the front axle is surely larger than that of the rear axle in vehicle under-steering $(\alpha_f > \alpha_r)$, the lateral tire force of the front axle enters the nonlinear region more quickly. Fig. 8(b) shows that the cornering stiffness values of both front and rear axles are changed according to the fluctuation of a_y in Fig. 8(a). Especially, that of front axle certainly drops to below the initial value. But, this sine steering maneuver makes the cornering stiffness less vigorously changed than other test maneuvers. The final weighting factor in Eq. (31) is generated, as shown in Fig. 8(c). Fig. 9 compares the sideslip angle estimation results obtained by the integrated observer, open-loop estimator, bicycle model and kinematic model-based EKFs. The kinematic model-based EKF prevents the integration drift of the open-loop estimator, but it still has noticeable deviations from the actual values. In this experimental case, the integrated observer generally gives more weight to the bicycle model-based EKF. When the bicycle model-based EKF estimates the incorrect values unexpectedly (at 7 s and 11.5 s), the increment of weighting factor leads the integrated observer to keep the high accuracy. Consequently, it is apparent that the integrated observer yields the most accurate estimation results. Unlike the other EKFs, the integrated observer using the proper weighting factor does not show any noticeable errors.

6.2.2. Experimental case 2

The DLC test is known as a typical handling test to look into the vehicle motion during extreme steering maneuvers. The severe steering and lateral acceleration profiles are shown in Figs. 10(a) and (b), respectively. Fig. 10(c) describes the abrupt changes of the cornering stiffness values. To prevent the cornering stiffness from unreasonably drifting away, ΔC_n is intentionally set to zero during intervals of steady state, such as 6–10 s. As can be seen in Fig. 10(c), $\Delta\hat{C}_{r,n}$ considerably smaller than $\Delta\hat{C}_{r,n}$ at the start of cornering (at 2.5 s and 12 s) distinctly indicates the under-steering tendency that the test vehicle lacks cornering agility. Also noteworthy, the transient states are clearly revealed in this experimental case. During the first DLC maneuver, $\Delta\hat{C}_{f,n} > \Delta\hat{C}_{r,n}$ (during 2–3.5 s, 4–5.5 s, and 6–8 s) and $\Delta\hat{C}_{r,n} > \Delta\hat{C}_{f,n}$ (during 3.5–4 s and 5.5–6 s) occur alternately. Surely, the second DLC maneuver shows similar trends. These are caused by the steering angle rate vigorously changed in the DLC test.

Compared with the previous case, the weighting factor in Fig. 10(d) changes more significantly. In doing so, it quickly induces the integrated observer to give more weight to the more appropriate vehicle model at each moment. Furthermore, both longitudinal velocity and heading angle are accurately estimated, as shown in Figs. 10(e) and (f). Actually, it is known that the sideslip angle estimation in the DLC test is

Fig. 6. Experimental set-up.

Table 2
The test scenarios.

Case	Driving maneuver	Typical longitudinal velocity	Type of road surface
1	Sine steer	70 km/h	Dry asphalt ($\mu \approx 1$)
2	Double lane change (DLC)	65 km/h	Dry asphalt
3	Acceleration in turn (AIT) + Long circle turn: 25 m of radius of gyration	35 km/h	Dry asphalt
4	AIT + Short circle turn: 15 m of radius of gyration	35 km/h	Dry asphalt
5	Brake in turn (BIT)	50 km/h	Packed snow ($\mu \approx 0.3$)

quite difficult. As can be seen from Fig. 11, the bicycle model is inadequate to track the rapidly varying actual sideslip angle. To tackle this difficulty, the integrated observer gives weights to the kinematic model based-EKF to a great extent, which is advantageous in the transient states. Instead, the bicycle model based-EKF prevents the estimation performance of the integrated observer from deteriorating at both 6 s and 15.5 s. Thus, the integrated observer maintains acceptable levels of error throughout the whole DLC test.

6.2.3. Experimental case 3

On a circular track with a long radius of gyration (25 m), the driver increases the vehicle speed for the first 5 sec (with the maximum longitudinal acceleration of 0.2 g), then keeps it at constant speed after that. While keeping both the steering angle and the vehicle speed constant, the value of lateral acceleration is around 0.5 g (see Fig. 12(b)). As can be seen from Fig. 12(c), this under-steered turn causes the cornering stiffness of the front axle to drop more sharply

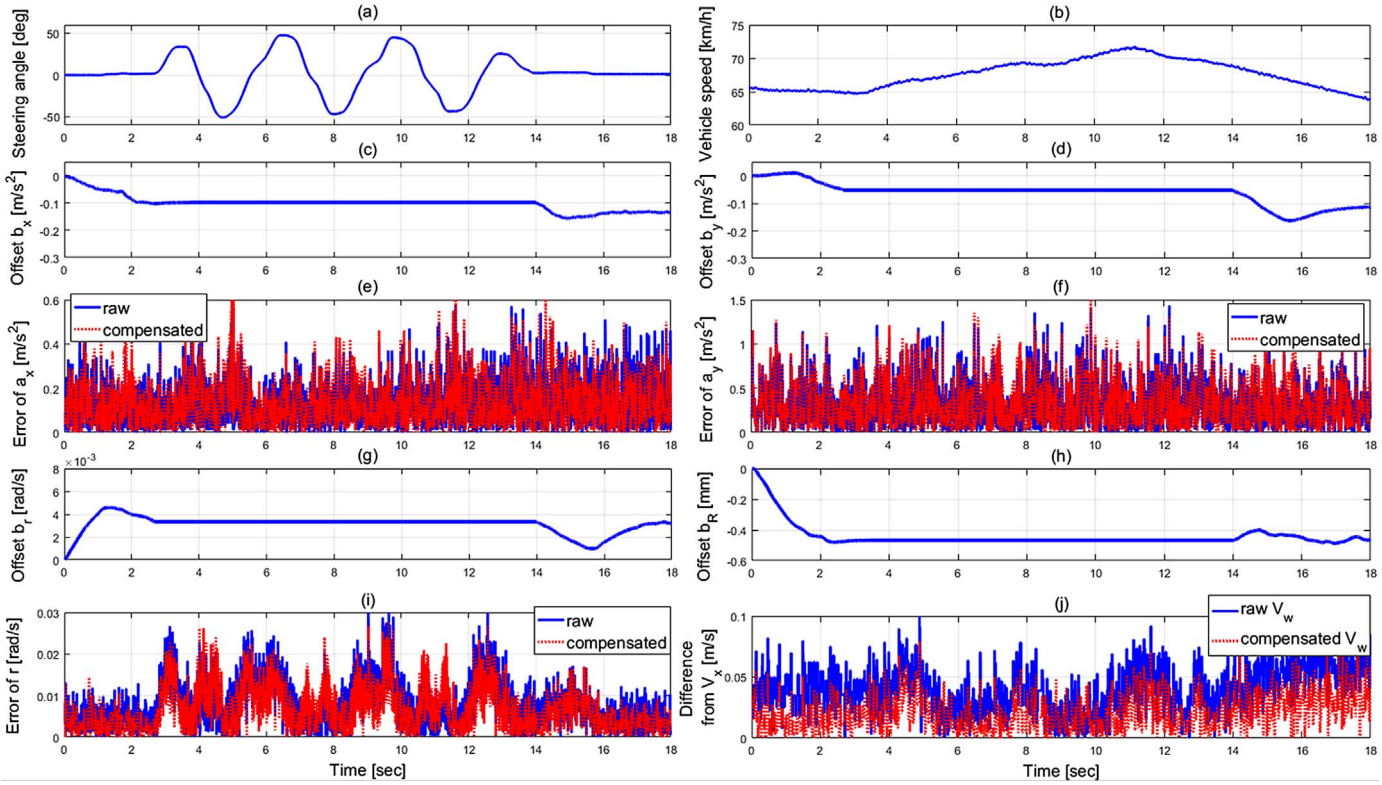

Fig. 7. Sine steer test results for sensor offset estimation: (a) Sine steer profile, (b) Vehicle speed profile measured by the GPS. Estimated offsets: (c) b_x, (d) b_y, (g) b_r and (h) b_R. Absolute errors of measurements: (e) a_x, (f) a_y and (i) r. (j) Absolute differences between actual v_x and v_w.

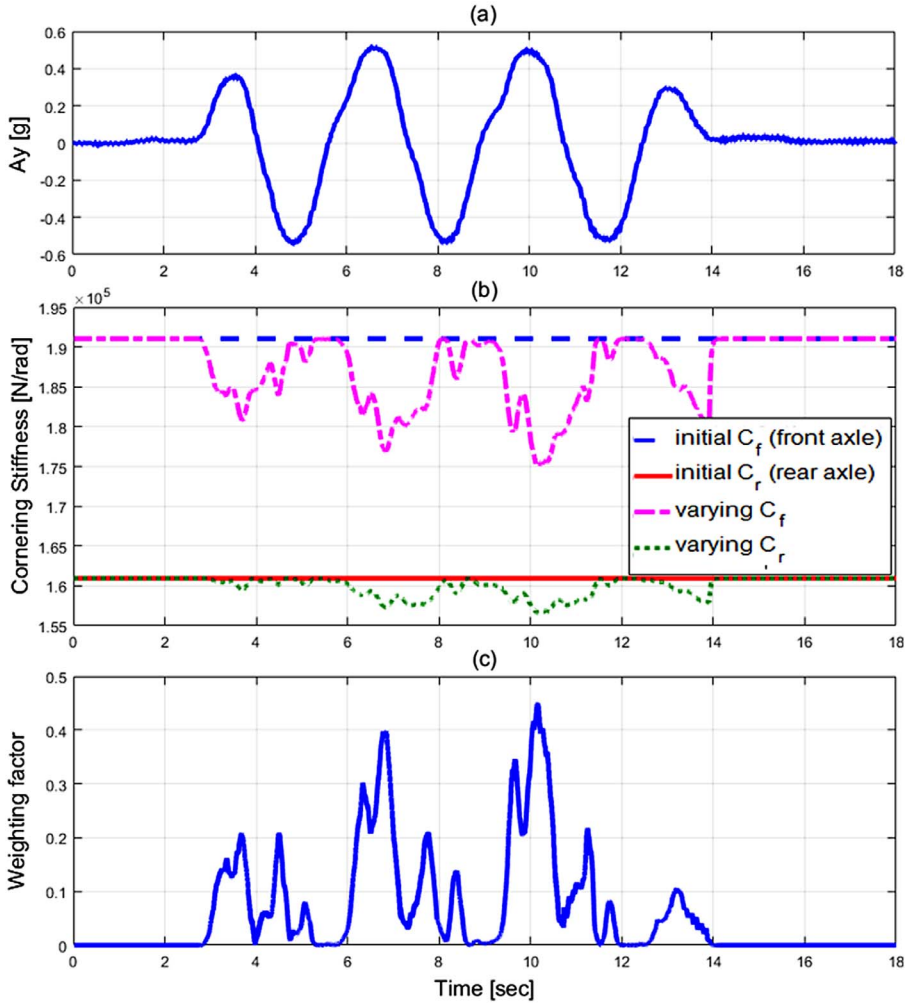

Fig. 8. Sine steer test results: (a) Lateral acceleration profile, (b) Cornering stiffness values of front and rear axles, (c) Weighting factor.

than that of the rear axle. For safety reason, most of passenger vehicles are designed to be under-steered in the steady state [17], so the results of Fig. 12(c) are reasonable. The driver's minute handle manipulation to follow the circular track in Fig. 12(a) causes the high frequency components of cornering stiffness estimation in Fig. 12(c). Since the centrifugal force is constant in the steady state of the circle turn, the sideslip angle is also maintained at a constant value in the steady state. Except for the open-loop estimator results fluctuating seriously, the other estimators show acceptable levels of errors, as shown in Fig. 13. Also, it is noteworthy that although the high-frequency components

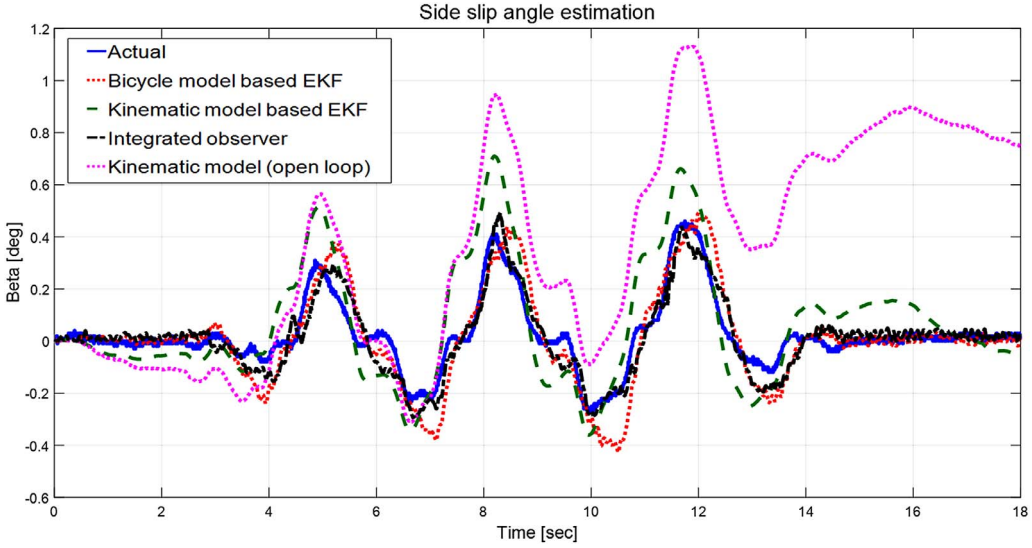

Fig. 9. Estimated sideslip angle during sine steer test.

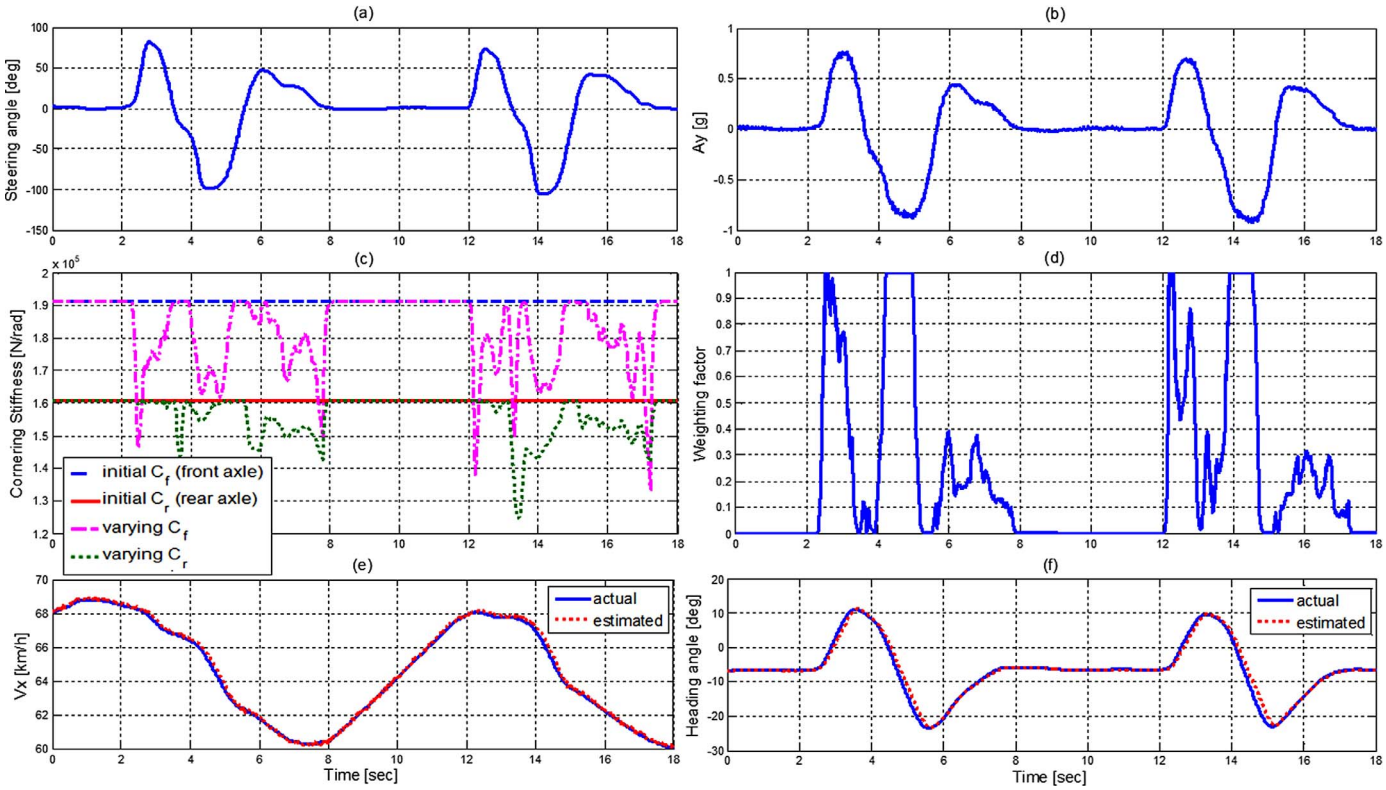

Fig. 10. DLC test results: (a) Sine steer profile, (b) Lateral acceleration profile. (c) Cornering stiffness values of front and rear axles. (d) Weighting factor. (e) Estimated longitudinal velocity, and (f) Estimated heading angle.

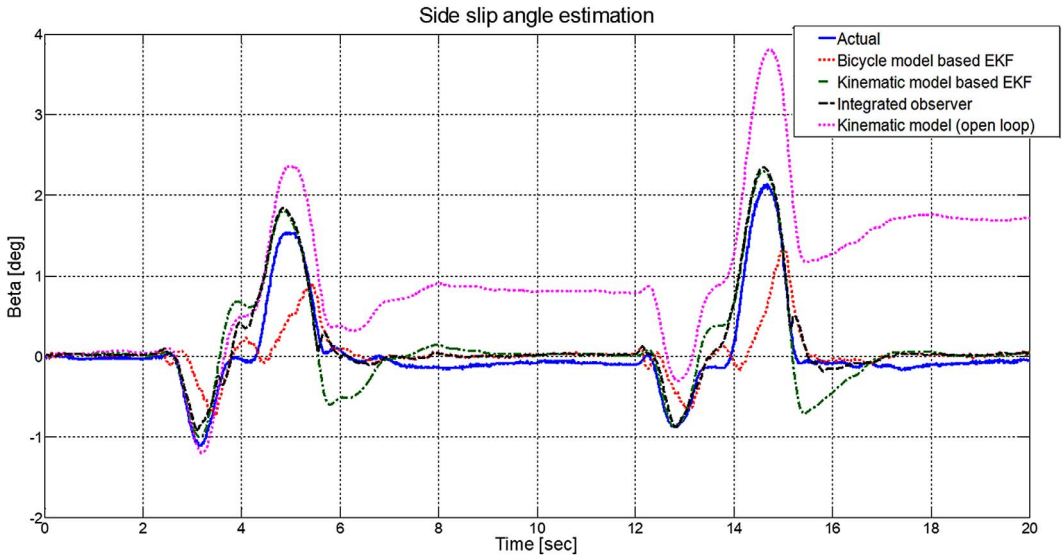

Fig. 11. Estimated sideslip angle during DLC test.

exist in both the cornering stiffness estimation and weighting factor (see Figs. 12(c) and (d)), the integrated observer provides relatively smooth estimation results by attenuating high-frequency signals: it is one of advantages of the integrated observer, as mentioned above.

6.2.4. *Experimental case 4*

For the first 10 sec, the longitudinal velocity increases from 20 km/h to 35 km/h. The maximum longitudinal acceleration is approximately 0.1 g. After that, a more severe circle turn than the previous case is performed: the radius of circle is shortened by 10 m, whereas the vehicle speed is almost the same. As shown in Fig. 14(b), the high lateral acceleration close to its limit implies the generation of a large sideslip angle. The lateral tire force of the front axle is expected to approach the saturation point, but that of the rear axle is not. The weighting factor in Fig. 14(d) sharply increases to 1, so that the kinematic model-based EKF exerts large influence on the final estimation results. Also, it is confirmed that the weighting factor is reduced to weight the bicycle model-based EKF at the end of the severe circle turn. Fig. 15 shows the high tracking performance of the integrated observer in both transient (during 0–10 s) and steady states (during 10–30 s). On the other hand, the other estimators have low accurate domains: the bicycle model-based EKF has noticeable steady state errors, and the kinematic model-

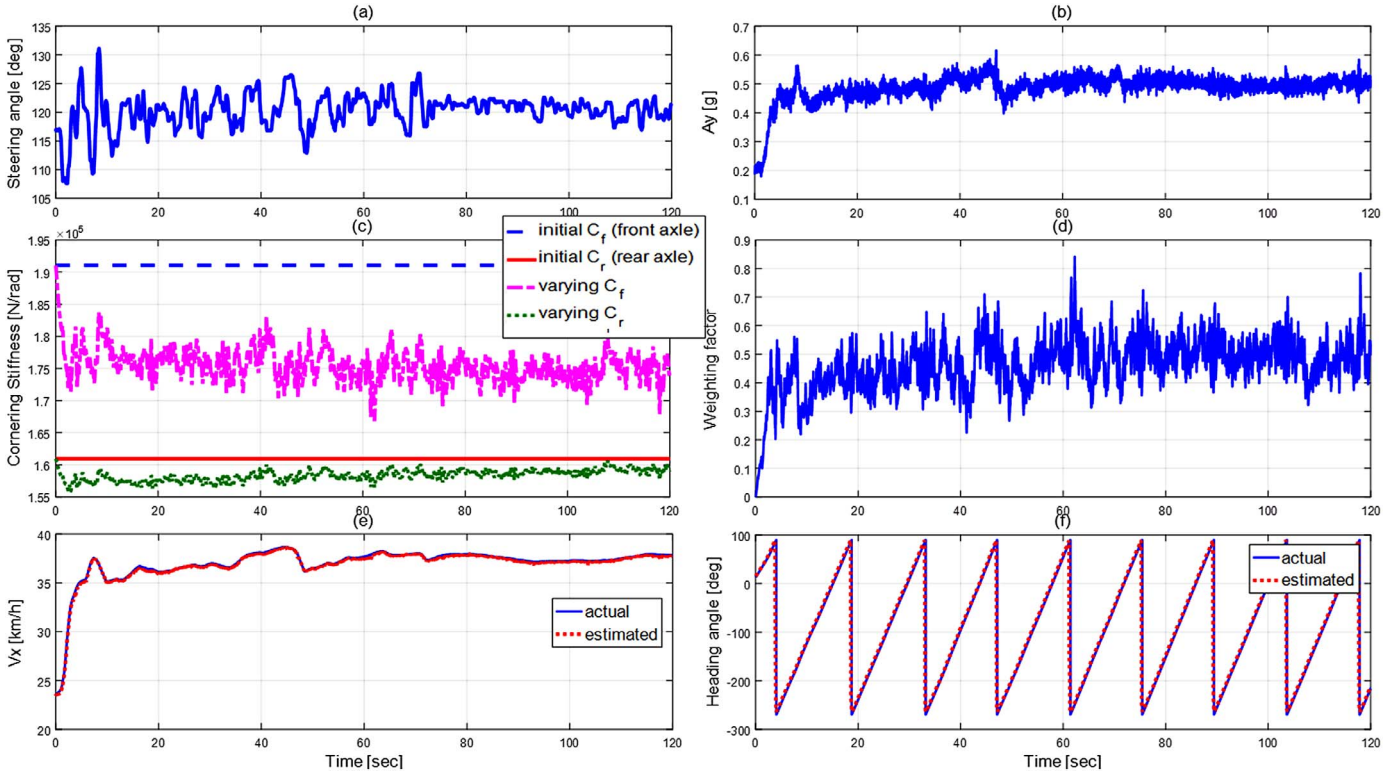

Fig. 12. Test results during AIT and long circle turn.

based EKF is less accurate at low vehicle speeds due to GPS characteristics.

6.2.5. *Experimental case 5*

During the first 4 seconds, the vehicle speed is increased to 50 km/h on the slippery road. At 5 s, the driver begins to perform both the braking and steering actions simultaneously. The maximum values of the vehicle deceleration and steering angle are 0.2 g and 200°, respectively. Since the safety control systems are intentionally deactivated to confirm the robustness of the estimation algorithm, the vehicle is spun out with the extremely excessive sideslip angle. Thus, the lateral acceleration in Fig. 16(b) is much larger than the TRFC ($\mu = 0.3$). As shown in Fig. 16(c), the initial cornering stiffness values are more decreased than those of previous cases ($\mu = 1$). During 7–9 s, they fall to near their minimum. Because of the wheel slip ratio in both acceleration and braking operations, the estimated vehicle speed has some slight differences from the actual value, as shown in Fig. 16(e).

It is shown in Fig. 17 that this BIT test causes the large sideslip angle reaching up to 50°: even if the steering angle returns to zero at 7.5 s, the sideslip angle is still large. But, due to the quickly increasing weighting factor in Fig. 16(d), the integrated observer can follow $v_{y,\,kin}$ rapidly and maintain the estimation performance even in this spin-out condition. In summary, the errors of the sideslip angle estimation based on the integrated observer approach are presented in Table 3. There are both maximum and root mean square (RMS) errors in each case. Table 3 shows the error levels that can be applied to production car applications.

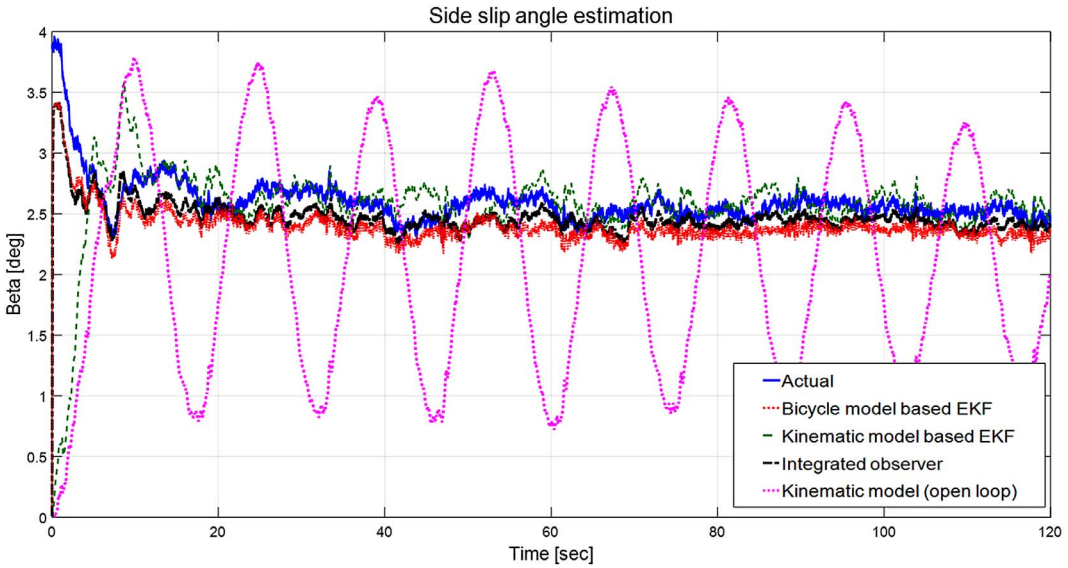

Fig. 13. Estimated sideslip angle during AIT and long circle turn tests.

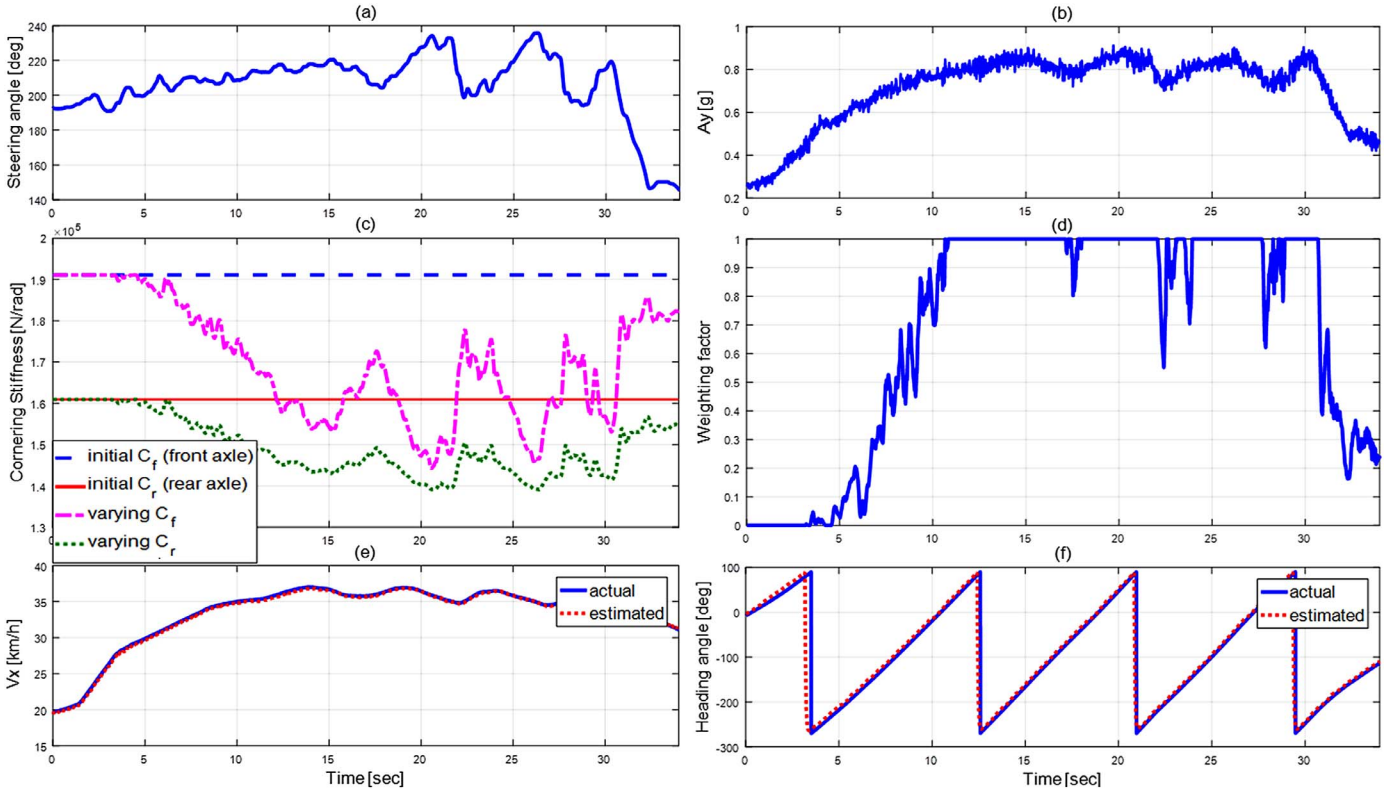

Fig. 14. Test results during AIT and short circle turn.

7. Conclusion

In this paper, a novel method has been proposed by which to estimate the various vehicle states, such as sideslip angle, heading angle, longitudinal velocity and tire cornering stiffness simultaneously. Three subsystems (sensor offset compensator, two vehicle model-based EKFs) are individually implemented using competitively priced sensor-fusion (in-vehicle sensors and GPS). Lastly, an integrated observer, based on novel weighting factor actively reflecting the real-time lateral dynamics, combines their estimation outputs. Through the real car-based experiments, high performance in estimation during various driving scenarios has been confirmed. The main contributions of the proposed algorithm are summarized as follows.

(1) The sensor offset compensator has a simple and intuitive structure, but it can easily eliminate the sensor intrinsic offset and improve the accuracy of the entire estimation algorithms.
(2) The bicycle model-based EKF with the tire cornering stiffness estimation provides the superior estimation performance in the tire linear region and detects the tire nonlinear region. In contrast, the kinematic model-based EKF solving the nonlinearity of the GPS measurements is usefully utilized in the tire nonlinear region.
(3) The final integrated observer has some advantages, such as higher estimation accuracy due to the prediction step of the EKF and

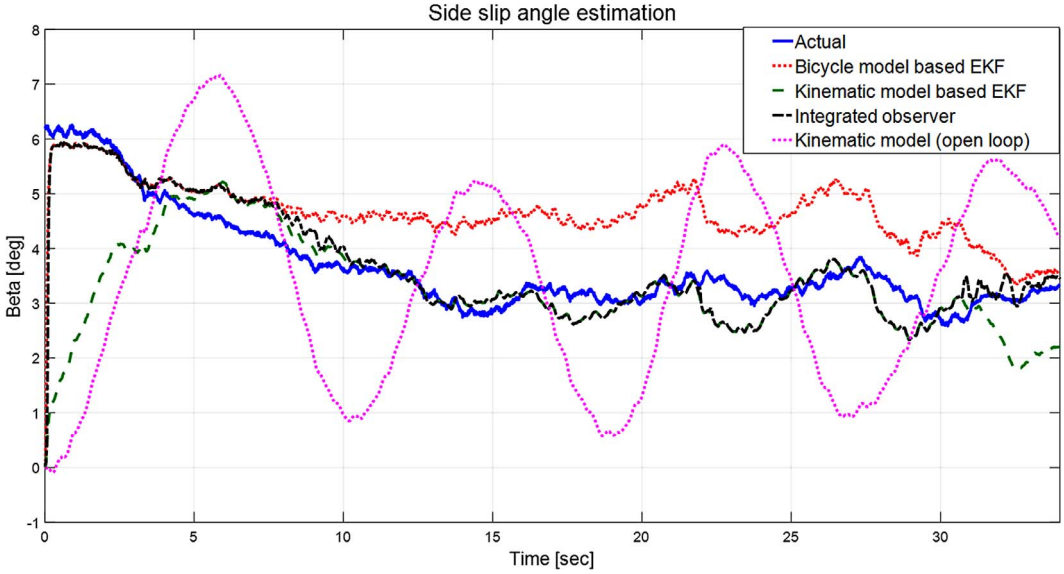

Fig. 15. Estimated sideslip angle during AIT and short circle turn tests.

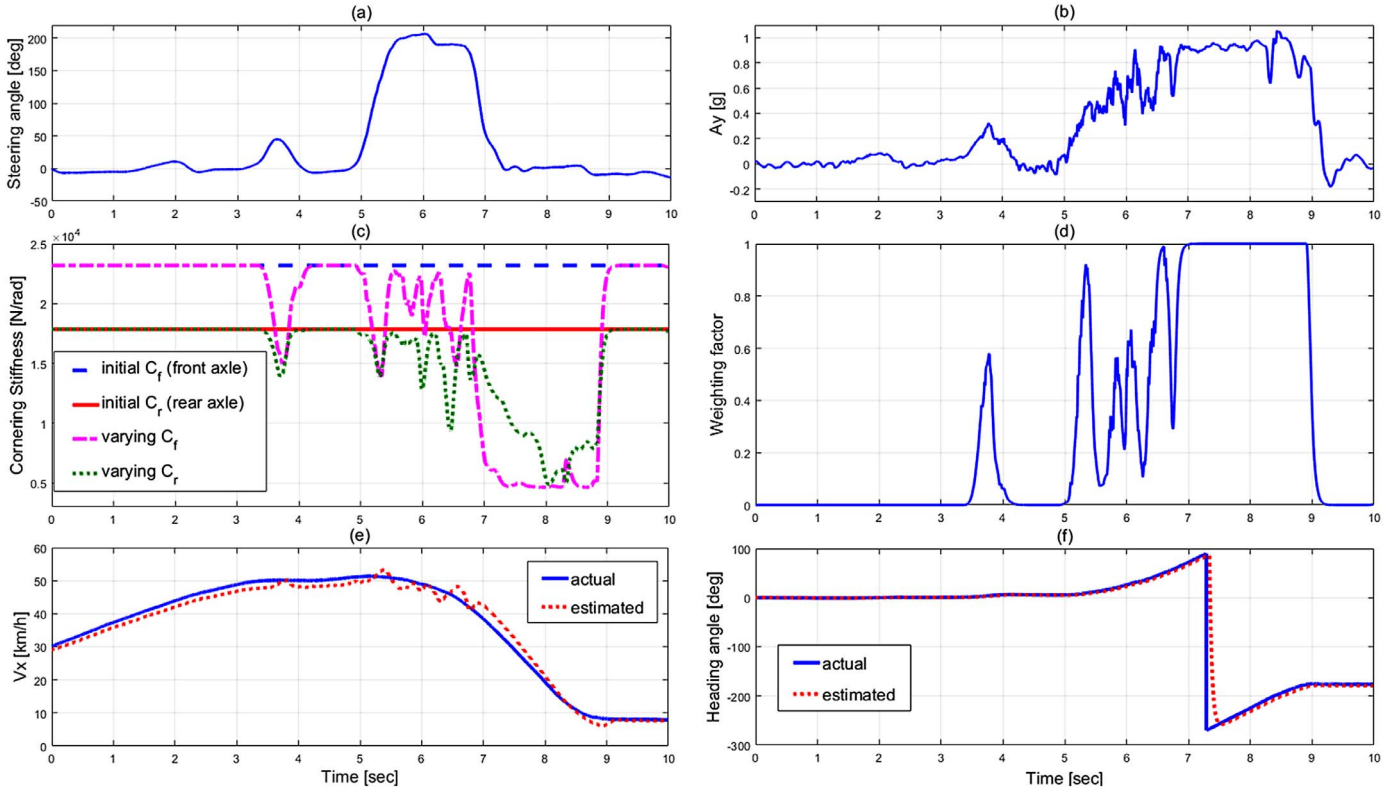

Fig. 16. Test results during BIT.

suppression of high-frequency noise without any phase lag issues.

(4) The proposed algorithm using only a minimal number of sensor signals is a cost-effective method.

(5) This paper demonstrates that the proposed algorithm can be a practical solution for vehicle state estimation of mass production vehicles. Also, it is expected that meaningful information provided by the proposed algorithm can be a promising tool to improve the performance of vehicle control systems.

Table 3
Errors of the sideslip angle estimation.

Case	Maximum error (°)	RMS error (°)
1	0.218	0.063
2	0.623	0.177
3	0.386	0.144
4	0.834	0.340
5	6.714	2.455

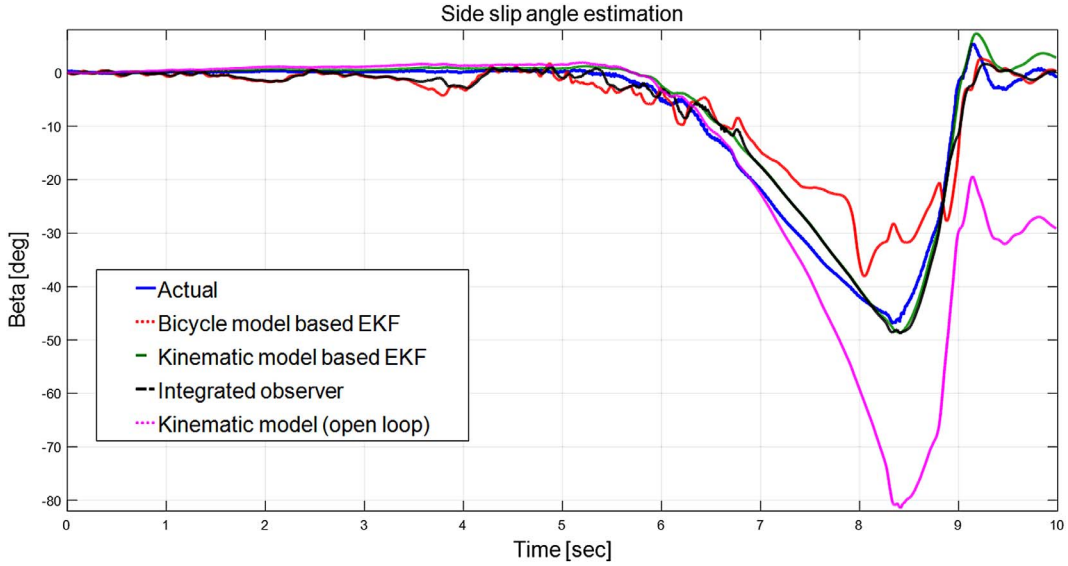

Fig. 17. Estimated sideslip angle during BIT test.

Acknowledgements

This work was supported by the National Research Foundation of Korea (NRF) grant funded by the Korea government (MSIP) (No.2017R1A2B4004116), the Technological Innovation R&D program of SMBA(S2341501), and the BK21 + program through the NRF funded by the Ministry of Education Korea. This research was supported by the MSIP (Ministry of Science, ICT and Future Planning), Korea, under the ITRC (Information Technology Research Center)support program (ITTP-2017-2012-0-00628) supervised by the ITTP (Institute for Information & communications Technology Promotion).

References

[1] Katriniok A, Abel D. Adaptive EKF-based vehicle state estimation with online assessment of local observability. IEEE Trans Control Syst Technol 2016;24(4):1368–81.
[2] Oh J, Choi S. Vehicle velocity observer design using 6-D IMU and multiple-observer approach. IEEE Trans Intell Transp Syst 2012;13(4):1865–79.
[3] Choi M, Choi S. Model predictive control for vehicle yaw stability with practical concerns. IEEE Trans Veh Technol 2014;63(8):3539–48.
[4] Doumiati M, Victorino A, Charara A, Lechner D. Onboard real-time estimation of vehicle lateral tire–road forces and sideslip angle. IEEE Trans Mechatronics 2011;16(4):601–14.
[5] Jo K, Chu K, Sunwoo M. Interacting multiple model filter-based sensor fusion of GPS with in-vehicle sensors for real-time vehicle positioning. IEEE Trans Intell Transp Syst 2012;13(1):329–43.
[6] Leung K, Whidborne J, Purdy D, Barber P. Road vehicle sate estimation using low-cost GPS/INS. Mech Syst Signal Process 2011;25(6):1988–2004.
[7] Han J, Rajamani R, Alexander L. GPS-based real-time identification of tire–road friction coefficient. IEEE Trans Control Syst Technol 2002;10(3):331–43.
[8] Hsu Y, Laws S, Gerdes J. Estimation of tire slip angle and friction limits using steering torque. IEEE Trans Control Syst Technol 2010;18(4):896–907.
[9] Nam K, Fujimoto H, Hori Y. Lateral stability control of in-wheel-motor-driven electric vehicles based on sideslip angle estimation using lateral tire force sensors. IEEE Trans Veh Technol(o) 2012;61(5):1972–85.
[10] Ryu J, Gerdes J. Integrating inertial sensors with global positioning system (GPS) for vehicle dynamics control. ASME J Dyn Syst Meas Control 2004;126(2):243–54.
[11] Cheli F, Sabbioni E, Pesce M, Melzi S. A methodology for vehicle sideslip angle identification: comparison with experimental data. Veh Syst Dyn 2007;45(6):549–63.
[12] Chen B, Hsieh F. Sideslip angle estimation using extended Kalman filter. Veh Syst Dyn 2008;46:353–64.
[13] Piyabongkarn D, Rajamani R, Grogg J, Lew J. Development and experimental evaluation of a slip angle estimator for vehicle stability control. IEEE Trans Control Syst Technol 2009;17(1):78–88.
[14] Park G, Hwang Y, Choi S. Vehicle positioning based on velocity and heading angle observer using low-cost sensor fusion. ASME J Dyn Syst Meas Control 2017;139(12):1–13.
[15] Yoon J, Peng H. A cost-effective sideslip estimation method using velocity measurements from two GPS receivers. IEEE Trans Veh Technol 2014;63(6):2589–99.
[16] Boada B, Boada M, Diaz V. Vehicle sideslip angle measurement based on sensor data fusion using an integrated ANFIS and an unscented Kalman filter algorithm. Mech Syst Signal Process 2016;72-73:835–45.
[17] Bevly D. Global positioning system (GPS): a low-cost velocity sensor for correcting inertial sensor errors on ground vehicles. ASME J Dyn Syst Meas Control 2004;126(2):255–64.
[18] Meguro J, Kojima Y, Suzuki N, Teramoto E. Positioning technique based on vehicle trajectory using GPS raw data and low-cost IMU. Int J Auto Eng 2012;3:75–80.
[19] You S, Hahn J, Lee H. New adaptive approaches to real-time estimation of vehicle sideslip angle. Control Eng Pract 2009;17:1367–79.
[20] Jo K, Lee M, Sunwoo M. Road slope aided vehicle position estimation system based on sensor fusion of GPS and automotive onboard sensors. IEEE Trans Intell Transp Syst 2016;17(1):250–63.
[21] Rajamani R. Vehicle dynamics and control. New York: Springer; 2006.
[22] Hashemi E, Pirani M, Khajepour A, Kasaiezadeh A, Chen S, Litkouhi B. Corner-based estimation of tire forces and vehicle velocities robust to road conditions. Control Eng Pract 2017;61:28–40.
[23] Baffet G, Charara A, Lechner D. Estimation of vehicle sideslip, tire force and wheel cornering stiffness. Control Eng Pract 2009;17:1255–64.
[24] Han K, Lee E, Choi M, Choi S. Adaptive scheme for the real-time estimation of tire-road friction coefficient and vehicle velocity. IEEE Trans Mech 2017;22(4):1508–18.
[25] Gadola M, Chindamo D, Romano M, Padula F. Development and validation of a Kalman filter-based model for vehicle slip angle estimation. Veh Sys Dyn 2014;52(1):68–84.
[26] Simon D. Optimal state estimation. New York: Wiley; 2006.
[27] Hermann R, Krener A. Nonlinear controllability and observability. IEEE Trans Auto Con 1977;22(5):728–40.
[28] Franklin G, Powell J, Naeini A. Feedback control of dynamic systems. 6th ed New York: Upper Saddle River; 2005.
[29] Pacejka H. Tire and vehicle dynamics. Oxford: Elsevier; 2005.
[30] Oh J, Choi S. Vehicle roll and pitch angle estimation using a cost-effective six-dimensional inertial measurement unit. IMechE D: J Automob Eng 2013;227(4):577–90.
[31] Reif K, Gunther S, Yaz E, Unbehauen R. Stochastic stability of the discrete-time extended Kalman filter. IEEE Trans Autom Control 1999;44(4):714–28.
[32] Li B, Du H, Li W, Zhang Y. Side-slip angle estimation based lateral dynamics control for omni-directional vehicles with optimal steering angle and traction/brake torque distribution. Mechatronics 2015;30:348–62.
[33] Park G, Choi S, Hyun D. Clamping force estimation based on hysteresis modeling for electro-mechanical brakes. Int J Autom Technol 2017;18(5):883–90.
[34] Yoon J, Li S, Ahn C. Estimation of vehicle sideslip angle and tire-road friction coefficient based on magnetometer with GPS. Int J Autom Technol 2016;17(3):427–35.
[35] Park G, Choi S, Hyun D. Clamping force estimation based on hysteresis modeling for electro-mechanical brakes. Int J Automot Technol 2017;18(5):883–90.
[36] Han K, Choi M, Lee B, Choi S. Development of a traction control system using a special type of sliding mode controller for hybrid 4WD vehicles. IEEE Trans Vehi Technol 2018;67(1):264–74.

Giseo S. Park received the B.S. degree in mechanical engineering from Hanyang University, Seoul, Korea, in 2014 and the M.S. degree in mechanical engineering from Korea Advanced Institute of Science and Technology (KAIST), in 2016. He is currently a Ph.D. candidate of mechanical engineering department at KAIST. His research interests include vehicle dynamics, control and active safety systems.

Seibum B. Choi received the B.S. degree in mechanical engineering from Seoul National University, Seoul, Korea; the M.S. degree in mechanical engineering from Korea Advanced Institute of Science and Technology (KAIST), Daejeon, Korea; and the Ph.D. degree in controls from the University of California, Berkeley, CA, USA, in 1993.

Since 2006, he has been with the faculty of the Department of Mechanical Engineering, KAIST. His research interests include fuel-saving technology, vehicle dynamics and control, and active safety systems.

Dongyoon Hyun received his B.S. and M.S. degrees in Agricultural Mechanical Engineering from Seoul National University. He began his graduate studies again in 1996 and received his M.S. and Ph.D. degrees in Mechanical Engineering from Texas A&M University in 1997 and 2001, respectively. Since 2003, he has worked as a senior research engineer at Hyundai-Kia R&D Center, and has been responsible for developing advanced chassis control systems.

Jounghee Lee received the Bachelor's degree in mechanical engineering from Yonsei University, Seoul, Korea, in 2009. Currently, He is with the Chassis System Control Development Team, Hyundai Motor Company, Hwaseong, Korea. His research interests include integrated control systems in chassis and intelligent vehicle safety systems.